Retrieval of Ocean Wave Spectra and RAR MTFs from Dual-Polarization SAR Data

G. Engen *   P.W. Vachon †   H. Johnsen *   F.W. Dobson ‡

30 June 1999

Abstract

A method for the retrieval of the real aperture radar (RAR) modulation transfer function (MTF) and ocean wave spectra from dual-polarization (*i.e.* simultaneously acquired HH and VV polarizations) synthetic aperture radar (SAR) image data is described. The RAR MTF is estimated by applying empirical MTF estimation methodologies to inter-look cross spectra between various combinations of individual looks and available polarizations for a given radar frequency. The concept behind the non-linear inversion is that any combination of like- and cross-polarization image spectra should return the same wave spectrum, in agreement with *in situ* and model wave spectra. This permits estimation of the RAR MTF on a case-by-case basis. The results are compared with theoretical treatments of the RAR MTF, which are shown to be inadequate for the range of conditions encountered in our data set. However, the theory and measurements fit well in describing the polarization dependence of the RAR MTF. The data set consists of SIR-C/X-SAR L-band and CCRS CV-580 C-band SAR data, *in situ* buoy measurements, and model data from field programs in Canadian waters in October and December, 1994.

*Norut Information Technology, N-9291 Tromsø Norway

†Canada Centre for Remote Sensing, 588 Booth St., Ottawa, Ontario K1A 0Y7 Canada

‡Fisheries and Oceans Canada, Bedford Institute of Oceanography, P.O. Box 1006, Dartmouth, Nova Scotia B2Y 4A2 Canada

Contents

List of Figures

List of Tables

1 Introduction

The derivation of the closed-form expression for the ocean-to-synthetic aperture radar (SAR) spectral transform [11, 17] and the formulation of an inversion scheme [11, 6, 18, 12] has increased the potential for oceanographic applications of SAR data. These schemes have been used over large scales for the inversion of ERS SAR data on a near operational basis [4, 3]. A weakness in these procedures is that they require *a priori* knowledge of the wave field and of the forward mapping transfer functions. *A priori* knowledge of wave field is required to resolve the 180°ambiguity in wave propagation direction, which is inherent in SAR images, while the transfer functions are required for correctly modelling the forward mapping.

Recently, the cross-spectrum methodology, in which the cross spectrum between individual SAR looks replaces the usual SAR image spectrum, was proposed and demonstrated for SAR data [7]. This methodology removes the propagation direction ambiguity by taking advantage of wave propagation over the short time interval between looks [26]. For example, a time separation of 0.37 s is achievable for the ERS SAR configuration, which yields a significant phase shift for the dominant ocean wave lengths of interest. Furthermore, it removes the speckle noise contribution to the SAR image spectrum [8], which simplifies the SAR inversion scheme, even for polar orbiting C-band SAR data, since the speckle is uncorrelated between the individual looks.

A key outstanding problem in the SAR imaging of ocean waves and in SAR image spectrum inversion, is the estimation of the real aperture radar (RAR) modulation transfer function (MTF). This function describes the modulation of the radar cross section by the long waves, and depends on the long waves themselves, the wind stress, the wave/wind imaging geometry, and the radar frequency and polarization. The RAR MTF is usually divided into a hydrodynamic component, a tilt component, and a range-shift component [21]. The hydrodynamic component arises from the modulation of the wave spectrum at the Bragg wavenumber, while the tilt and range-shift components are purely geometrical effects. The RAR MTF contributes significantly to the imaging process for waves travelling in the near range direction and is, therefore, an important factor for a proper inversion of the SAR data. The RAR MTF has often been measured using tower-mounted radars [22, 10]. More recently, however, the RAR MTF has been estimated by using actual SAR data through simulation [5] or by direct measurement from a SAR image spectrum [13]. Comparison of measured results with models based on composite surface theory [15, 10, 23] indicate some consistency. However, it is apparent that not all RAR MTF measurements can be explained by existing theoretical formulations.

With the development of SAR instrumentation and the increased availability of multi-channel (*i.e.* multi-polarization and/or multi-frequency) SAR data, a further improvement in the inversion of SAR data can be achieved. In this paper, we extend the cross-spectrum inversion procedure to the case of multi-polarization SAR data. In so doing, it is also shown that multi-polarization SAR data can provide additional information concerning the RAR MTF.

The paper is arranged as follows. In Section 2, the theory of the ocean-to-SAR cross-spectrum transform is described for the general case of multi-channel SAR data. The standard theoretical expressions for the RAR MTFs are also presented. In Section 3, the multi-channel SAR data sources and validation data sets, along with the data analysis methodology are described. In Section 4, the results of the RAR MTF analysis and the inversion of dual-polarization SAR data are presented.

2 Theory

2.1 The Ocean-to-SAR Image Cross-Spectrum Transform

In this section, a theoretical expression for the ocean-to-SAR image cross-spectrum transform for the general case of multi-channel SAR images is developed. Let $\mathbf{x} = (x, y)$ represent a position vector in the backscatter image $I_n(\mathbf{x}, t)$, $n \in \mathcal{N}$, where $\mathcal{N}$ is the set of different channels, x is azimuth, y is ground range, and t is time. Then, in the non-dispersive case, the SAR image can be written as:

$$I_n^{\mathrm{s}}(\mathbf{x}', t) = \int d\mathbf{x}\, I_n(\mathbf{x}, t)\, \delta(\mathbf{x} - \boldsymbol{\xi}(\mathbf{x}, t) - \mathbf{x}') \ , \quad n \in \mathcal{N} \, , \tag{1}$$

where $\boldsymbol{\xi} = (\xi_x, \xi_y)$ is the shift vector caused by the surface elevation ζ, and the slant-range component U_r of the wave orbital velocity:

$$\xi_x(\mathbf{x}, t) = \frac{\zeta(\mathbf{x}, t)}{\tan\theta} \tag{2}$$

$$\xi_y(\mathbf{x}, t) = \frac{R}{V}\, U_r(\mathbf{x}, t)\, . \tag{3}$$

where θ is the incidence angle, R is the slant-range distance from the radar to the wave-field, and V is the radar platform velocity. The extension to the dispersive case is straightforward [18]. I_n is the backscatter image, which is distinct from the RAR image which also includes the large scale range bunching effects.

Following the formalism of [11, 17, 7], the different SAR image cross spectra P_{mn}, $(m, n) \in \mathcal{N}$, can be written as

$$
\begin{aligned}
P_{mn}(\mathbf{k}, \tau) &= \int d\mathbf{x}\, e^{k_x^2 \mu_{xx} + k_y^2 \mu_{yy} + k_x k_y (\mu_{xy} + \mu_{yx})} \{ 1 + \rho_{mn} \\
&+ ik_x(\mu_{mx} - \mu_{xn}) + ik_y(\mu_{my} - \mu_{yn}) \\
&+ (k_x\, \mu_{mx} + k_y\, \mu_{my})(k_x\, \mu_{xn} + k_y\, \mu_{yn}) \} \qquad (4)
\end{aligned}
$$

where $\rho_{mn} \equiv \rho_{mn}(\mathbf{x}, \tau)$, $\mu_{ab} \equiv \rho_{ab}(\mathbf{x}, \tau) - \rho_{ab}(\mathbf{0}, 0)$, $\mathbf{k} = (k_x, k_y)$, and τ is the time seperation between the pair of looks. The various covariance functions are related to the modulation transfer functions T_a and T_b and to the ocean wave spectrum S through

$$
\rho_{ab}(\mathbf{x}, \tau) = \mathrm{Re} \left\{ \tfrac{1}{(2\pi)^2} \int e^{i\mathbf{k}\cdot\mathbf{x} - i\omega_k \tau}\, T_a(\mathbf{k})\, T_b^*(\mathbf{k})\, S(\mathbf{k}) \right\} , \qquad (5)
$$

where $\omega_k \tau$ is the phase shift that the wavenumber component with frequency $\omega_k = \sqrt{g|\mathbf{k}|}$ undergoes during the time interval τ. The lower indices x, y, m, and n, used on the right side of equation (4), refer to ξ_x, ξ_y, $\frac{I_m}{\mathrm{E}\{I_m\}}$, and $\frac{I_n}{\mathrm{E}\{I_n\}}$, respectively. We denote the respective transfer functions as T_x,T_y,T_m, and T_n. These are defined later in equations (6) to (9).

The model for the SAR cross covariance spectrum given by equation (4) can be used to solve for the ocean wave spectrum S if the backscatter MTF's T_n, $n \in \mathcal{N}$ are known [7]. When this is the case, there exists a unique solution in the area $\mathbf{k} \in \mathrm{I\!R} \times [-k_c, k_c]$, defined by the positive azimuth wavenumber $k_c \ll \rho_{yy}^{-1/2}(\mathbf{0}, 0)$, which relates the ocean wave spectrum linearly to the SAR image cross spectrum [17]:

$$
\begin{aligned}
P_{mn,\tau}(\mathbf{k}, t) &\approx \tilde{T}_m(\mathbf{k})\, \tilde{T}_n^*(\mathbf{k})\, e^{-i\omega_k t}\, S(\mathbf{k}) \\
&+ \tilde{T}_m^*(-\mathbf{k})\, \tilde{T}_n(-\mathbf{k}))\, e^{i\omega_k t}\, S(-\mathbf{k}) \qquad (6) \\
\tilde{T}_m(\mathbf{k}) &= ik_x\, T_x(\mathbf{k}) + ik_y\, T_y(\mathbf{k}) + T_m(\mathbf{k}) \qquad (7)
\end{aligned}
$$

where $m, n \in \mathcal{N}$. Since, the set of SAR image cross spectra of equation (4) must reflect the same ocean wave-spectrum S, the possible choices of backscatter MTF's are constrained. With reasonable models for the bacskatter MTF's, this constraint allows us not only to treat the wave spectrum, but also the free parameters of the backscatter MTF's, as unknowns in an inversion scheme. In fact, the combination of poorly known backscatter MTF and multi-channel SAR data requires a coupled backscatter MTF and ocean wave spectrum estimation procedure in order to produce a consistent solution of the inversion problem, *i.e.* a single wave spectrum that reflects the entire SAR data set.

2.2 The RAR MTF

According to linear wave theory, the range [9] and azimuth [2] shift modulation transfer functions are

$$\begin{aligned} T_x(\mathbf{k}) &= \frac{1}{\tan\theta} && (8) \\ T_y(\mathbf{k}) &= \frac{R}{V}\,\omega_k \left\{ \frac{k_x}{|\mathbf{k}|}\sin\theta + i\cos\theta \right\} . && (9) \end{aligned}$$

These expressions are used in the RAR MTF estimation algorithm, described in Section 4.2, and in the non-linear inversion algorithm, described in Section 4.3. The following expressions for the backscatter MTF's (which are the RAR MTF's subtracted from the range bunching MTF: $ik_x T_x$) are given here as a basis for later discussion.

By applying the Bragg approximation for the short waves in a two-scale model and by using the geometric optical solution for a perfect conducting surface, the linear backscatter MTF can be separated into two parts: first, the geometrical MTF caused by the surface tilting; and second, the hydrodynamic MTF caused by surface straining. Based on these assumptions, the tilt MTF is [20]:

$$T_m^{\mathrm{tilt}}(\mathbf{k}) = ik_x \frac{4 - 0.5(1 + s_m \sin^2\theta)}{\tan\theta(1 + s_m \sin^2\theta)} , \tag{10}$$

which is strictly imaginary and is polarization dependent since

$$s_m = \begin{cases} -1, & \text{for VV polarization} \\ 1, & \text{for HH polarization.} \end{cases} \tag{11}$$

An expression which is commonly used for the hydrodynamic MTF [1] is based on weakly non-linear wave-wave interaction theory, and arises from the modulation of the Bragg-scale waves by the orbital velocity of the longer waves:

$$T^{\mathrm{hydr}}(\mathbf{k}) = 4\,\frac{\omega_k - 2i\beta}{\omega_k^2 + 4\beta^2}\;\frac{\omega_k k_x^2}{|\mathbf{k}|} , \tag{12}$$

where β is the wind growth-rate of the Bragg waves. According to equations (8) to (12), the polarization dependence enters only through the tilt contribution. However, recent theoretical studies and tower measurements suggest a weak polarization dependence of the hydrodynamic contribution [23].

3 Data

The SAR data considered in this paper were acquired by two different radars during two different field campaigns in Canadian waters.

3.1 SIR-C/X-SAR

During the second shuttle imaging radar (SIR) mission of SIR-C/X-SAR [14, for example] in October 1994, we deployed a meteorological buoy (referred to as MiniMet - MM) and a directional wave buoy (a Datawell Directional Wave Rider - DWR) in the Gulf of St. Lawrence, south of Iles de la Madeleine (Fig. 1). There were six SIR-C/X-SAR datatakes in the vicinity of the buoys, providing us with multi-frequency, multi-polarization SAR imagery and calibrated wind and wave data for validation purposes (see Fig. 1 and Table 1). In addition, the Canadian Spectral Ocean Wave Model (CSOWM) [16] was run in hindcast mode for our region using Canadian Meteorological Centre (CMC) model winds.

In Fig. 2, we present time series of wind speed and significant wave height from CSOWM for grid point 3708 and from the nearby buoy location, for the duration of the SIR-C/X-SAR mission. The wind speeds and wave heights are seen to have been in the low to moderate range. The agreement between the model and the buoy measurements is good. However, it is worth noting that the CMC wind field missed peak wind events on Oct. 3 and Oct. 4. Therefore, CSOWM did not predict the corresponding peak wave height events. This is particularly relevant for the Oct. 3 event, during which datatake 49.33 occurred. In the present paper only SIR-C/X-SAR L-band data have been used since the X- and C-band data have too small an integration time to produce a significant imaginary part in their inter-look cross spectra (see Table 1).

3.2 CCRS CV-580

As part of ongoing SAR ocean validation efforts [25, 24], the Sea Truth and Remote Sensing (STARS) experiment was carried out from the Bedford Institute of Oceanography (BIO) research vessel CSS *Parizeau* in December 1994. As part of this project, we deployed MM and DWR buoys on the Grand Banks of Newfoundland near CSOWM grid points (Fig. 3). In addition to ERS-1 SAR image data, the Canada Centre for Remote Sensing (CCRS) CV-580 SAR [19] was deployed on three separate occasions, providing us with C-band dual-polarization (HH and VV) SAR imagery and calibrated wind and wave data for validation purposes (see Fig. 3 and Table 2). In addition, the 3rd generation CSOWM was run in hindcast mode using CMC model winds.

In Fig. 4, we present time series of wind speed and significant wave height from CSOWM for grid points which were nearby the buoy location, for the duration of STARS'94. The wind speeds and wave heights at the SAR acquisitions times are again in the low to moderate range. The agreement between the model and the buoy measurements is good. The buoy time series are limited in extent since the ship was disabled prior to the planned termination of the field program, which limited the overall data set.

4 Analysis

We now present the data analysis procedures carried out on the various available SAR data sets.

4.1 Cross Spectrum Estimation

In this paper we are considering SAR data from four separate radars, as summarized in Tables 1 and 2. In each case, the images were received in their respective single look complex (SLC) forms, that is, in slant-range/zero-Doppler coordinates with natural sampling intervals in slant-range ($c/2F$, where c is the speed of light and F is the analogue-to-digital converter sampling rate) and azimuth (V_p/PRF, where V_f is the footprint velocity and PRF is the radar pulse repetition frequency). In each case, a subscene in the vicinity of the buoy location was chosen and extracted from the full SLC product. The subscene was Fourier transformed, the Doppler centroid was found, and a set of L looks of bandwidth B_L were extracted, centred on the Doppler centroid and evenly distributed over the SAR azimuth bandwidth, B_p. Each extracted look was inverse transformed, detected, and converted to ground-range to provide a set of L individual looks. A pair of looks is separated in time from one another by [25]

$$\tau = \frac{\lambda R}{2V_p V_f} \Delta B \tag{13}$$

where λ is the radar wave length, R is the slant range to the centre of the scene of interest, V_p is the platform velocity, and ΔB is the frequency difference between the centres of the two looks.

SAR image cross spectra were calculated from all pairs of non-overlapping looks with fixed separation τ. The available cross spectra were then averaged together and smoothed to produce the final inter-look cross spectrum estimate. The right hand side of Tables 1 and 2 provide the information relevant to the selected subscenes and estimated cross spectra. For the SIR-C/X-SAR data, the X-band data are from a slightly different location than the C-band and L-band data. This is reflected in the two different incidence angles. The value of τ scales with λ, so three separate τ's are included.

The multiple channels were achieved by combining look pairs from separate polarizations. For example, the HH-HH channel is based on the HH polarization data alone, while the HH-VV channel is based on the combination of HH and VV data. All possible dual-polarization combinations were formed for the available channels at each frequency. Cross-polarization data was not considered due to their low signal-to-noise ratio. Our subsequent analysis focusses on the CV-580 STARS data set and the SIR L-band data. The latter include good signal-to-noise ratio and maximize the inter-look time step which improves the resolution of the wave propagation direction.

4.2 RAR MTF Estimation

The RAR MTF was estimated in the linear region of the SAR spectra, as defined in equation (6), using the four combinations available from HH and VV measurements *i.e.* $\mathcal{N} = HH, VV$. The models for the backscatter MTFs include the following constraints, reflecting the basic properties of the theoretical expressions of equation (10) and (12):

- Both MTFs are assumed to have the same real part:

$$\mathrm{Re}\{T_{\mathrm{HH}}(\mathbf{k})\} = \mathrm{Re}\{T_{\mathrm{VV}}(\mathbf{k})\}\,. \tag{14}$$

This is a good assumption in the limit of Bragg-scattering, for which only the imaginary tilt MTFs include polarization effects (*i.e.* in the two-scale model).

- Both MTFs are assumed to only be functions of range wavenumber:

$$T_n(\mathbf{k}) = T_n(k_x, 0) \ , \quad n \in \mathcal{N} \, . \tag{15}$$

Since the velocity-bunching transfer function, $ik_y \, T_y$, is likely to be much steeper in the azimuth direction than the backscatter MTFs, the zero-order azimuth term is the most important.

- The MTFs are constrained to have symmetrical real parts and asymmetrical imaginary parts:

$$T_n(\mathbf{k}) = T_n^*(-\mathbf{k}) \ , \quad n \in \mathcal{N} \, . \tag{16}$$

This is done so as not to favor any two wave systems of the same wave length that propagate in opposing directions.

- The MTF's are assumed to be “smooth” functions.

The following model satisfies the three first constraints:

$$T_n(\mathbf{k}) = |k_x| \, a(k_x) + ik_x \, b_n(k_x) \, . \tag{17}$$

In order to derive the RAR MTF, we minimize a cost function which includes the fourth constraint:

$$\begin{aligned} J \;\; = & \sum_{m,n \in \mathcal{N}} \int d\mathbf{k} \, \mathrm{Re}^2 \{ P_{mn}(\mathbf{k}) - P_{mn}^{\mathrm{obs}}(\mathbf{k}) \} \, W_{\mathrm{Re}}(\mathbf{k}) \\ + & \sum_{m,n \in \mathcal{N}} \int d\mathbf{k} \, \mathrm{Im}^2 \{ P_{mn}(\mathbf{k}) - P_{mn}^{\mathrm{obs}}(\mathbf{k}) \} \, W_{\mathrm{Im}}(\mathbf{k}) \\ + & \int dk_x \left\{ \left(\tfrac{\partial a}{\partial k_x}(k_x) \right)^2 + \sum_{n \in \mathcal{N}} \left(\tfrac{\partial b_n}{\partial k_x}(k_x) \right)^2 \right\} W(k_x) \end{aligned} \tag{18}$$

where P_{mn}^{obs} and P_{mn}, $m, n \in \mathcal{N}$, are the observed and computed SAR image cross spectra, respectively, and W_{Re}, W_{Im}, and W are positive weight functions, the first two having support in the azimuth direction only on the interval $k_y \in [-k_c, k_c]$.

The cost function is minimized by requiring that the partial derivatives with respect to all the free parameters be zero:

$$\frac{\partial J}{\partial S(\mathbf{k})} = 0 \ , \quad \frac{\partial J}{\partial a(k_x)} = 0 \ , \quad \frac{\partial J}{\partial b_n(k_x)} = 0 \, , \tag{19}$$

where $\mathbf{k} = (k_x, k_y) \in \mathrm{I\!R}^2$ and $n \in \mathcal{N}$. The minimization may be done numerically (*i.e.* by using a gradient method [7] since both $f(\mathbf{s}) = \frac{\partial J}{\partial \mathbf{s}}$ and ∇f, where $\mathbf{s} = (S, a, \{b_n\}_{n\in\mathcal{N}})$, may be derived analytically). The corresponding *HH* and *VV* RAR MTFs are then given as the sum of the estimated backscatter MTF and the range-bunching MTF: $ik_x T_x$.

4.3 Cross-Spectrum Inversion

The method used for the cross spectrum inversion is based on finding a wave spectrum which minimizes the cost-function:

$$\begin{aligned} J &= \int d\mathbf{k}\, \mathrm{Re}^2\{\bar{P}(\mathbf{k},\tau) - \bar{P}^{\mathrm{obs}}(\mathbf{k},\tau)\}\, W_{\mathrm{Re}}(\mathbf{k}) \\ &+ \int d\mathbf{k}\, \mathrm{Im}^2\{\bar{P}(\mathbf{k},\tau) - \bar{P}^{\mathrm{obs}}(\mathbf{k},\tau)\}\, W_{\mathrm{Im}}(\mathbf{k}) \end{aligned} \tag{20}$$

where $\bar{P}^{\mathrm{obs}}$ is the average observed SAR cross spectrum:

$$\bar{P}^{\mathrm{obs}}(\mathbf{k},,\tau) = \frac{1}{N_{\mathcal{N}}^2} \sum_{n,m\in\mathcal{N}} P^{\mathrm{obs}}_{mn}(\mathbf{k},t) \tag{21}$$

Here $N_{\mathcal{N}}$ is the number of channels. The averaging process is done in order to decrease the spectral uncertainty. The corresponding computed SAR spectrum, $\bar{P}$, is based on the non-linear expression for the SAR transform where we use the average RAR MTF:

$$T(\mathbf{k}) = \frac{1}{N_{\mathcal{N}}} \sum_{n\in\mathcal{N}} T_n(\mathbf{k}) = |k_x|\, a(k_x) + \frac{ik_x}{2} \sum_{n\in\mathcal{N}} b_n(k_x) \tag{22}$$

The following weight functions were used

$$W_{\mathrm{Re}}(\mathbf{k}) = 1 \tag{23}$$

$$W_{\mathrm{Im}}(\mathbf{k}) = \frac{\int d\mathbf{k}'\, \mathrm{Re}^2 \bar{P}^{\mathrm{obs}}(\mathbf{k}',\tau)}{\int d\mathbf{k}'\, \mathrm{Im}^2 \bar{P}^{\mathrm{obs}}(\mathbf{k}',\tau)}\,, \tag{24}$$

along with a gradient method [7] to minimize the cost-function of equation (20). Since the cross spectrum contains the propagation characteristics of the wave field, no *a priori* information is needed for initialization of the inversion process. The RMS errors between the computed and the observed cross spectra are used to ensure that a global minimum is achieved.

5 Results

5.1 RAR MTF

The RAR MTF was estimated using the metodology described in Section 4.2 using all of the data described in Section 3. The data covers different environmental conditions and Bragg wavenumbers. A typical example of the RAR MTF obtained is shown in Figure 5. The real and the imaginary parts of the RAR MTF for HH and VV polarizations are shown together with the difference between the imaginary parts of the HH and the VV data. The corresponding theoretical functions are also shown, based on the equations in Section 2.2. A summary of the RAR MTF measuements are listed in Table 3 across the full data set. The results show that the SAR tends to measure a higher amplitude than predicted by theory and that the deviation is largest for HH polarization. For the phase, the measured values are in most cases lower than the predicted values for both VV and HH data. However, the polarization dependency of the RAR MTF, shown by the difference in the imaginary part of the RAR MTF between VV and HH polarization, is in good agreement with theorectical predictions. This indicates that the polarization term of the total RAR MTF is well-described with the tilt contribution, as given in equation (10). This is also illustrated in Figure 6 for the spectral maxima. The observed discrepancy in the RAR MTF amplitude arises from the backscattering model being imperfect, which here is based on linear Bragg scattering theory.

5.2 Ocean Wave Spectra

The inversion results are presented in Figures 7 to 13. All of the details are presented for two of the data sets, while only the final results are shown for the rest. Figure 7 shows the observed and the best fit average cross spectra, as defined in equation (21), for one CV-580 C-band case. A similar plot for a SIR L-band case is shown in Figure 8. Inspection of these figures indicates that the simulated cross spectra, based on the final wave spectrum and the cross-spectrum transform, are in good agreement with the observed cross spectra. This verifies that global minima have been found during the minimization procedure. A summary of the inversion results is shown in Figures 9 and 10 in which the SAR-derived wave spectra are plotted together with the wave model and buoy spectra for all the cases analyzed. We see that the CV-580 C-band results (Figure 10) are very similar to the wave model data and to the buoy spectra, while the SIR L-band results show wave modes that are not present in the wave model output. This is especially apparent for the October 7 data. However, for October 7, the SIR L-band spectrum agrees resonably well with the DWR spectrum. The discrepancy between the SIR L-band, CSOWM, and DWR spectra in Figure 9 that is not observed for the CV-580 C-band data shown in Figure 10 may arise from problems with the wave modelling or wind field, from differences between the DWR and SAR spatial and temporal sampling, as well as from a low SNR for these SAR observations. The SNR difference effect can be addressed by noting that the CV-580 C-band cross spectra have a look separation time that is 4 times larger than that of the SIR L-band cross spectra (see Table 2 and Table 1), resulting in a much higher SNR for the imaginary part of the cross spectra. Possible problems with the wave modelling are beyond the scope of this paper.

Figure 11 shows the SAR-derived significant waveheights vs. *in situ* DWR waveheights. The CV-580 C-band waveheights fit well with the *in situ* measurments, while the SIR L-band waveheights are as much as 30% too low. This may be due to the relatively poor SNR of the SIR-C/X-SAR data.

Because of the coupled RAR MTF and wave spectrum estimation scheme, the final wave spectrum is able to reproduce all of the cross spectra within a single SAR acquisition (*i.e.* for all combinations of HH and VV polarizations). Sample results are shown in Figure 12 for CV-580 C-band data and in Figure 13 for SIR L-band data. Inspection of the figures indicates good agreement between the computed and the measured cross spectra for all combinations of HH and VV polarization.

6 Conclusions

In this paper, we have considered multi-frequency and multi-polarization SAR image data of ocean waves. The data were derived from two field programs in 1994: first, six SIR-C/X-SAR acquisitions near a wind/wave buoy site in the Gulf of St. Lawrence; and second, three CCRS CV-580 SAR acquisitions near a a wind/wave buoy site on the Grand Banks of Newfoundland. In each case, the SAR and *in situ* observations were complemented by hindcast wave model spectra.

The data sets were reduced to multi-channel inter-look cross spectra by bandpass filtering the SLC image products. The cross spectra were then subjected to a retrieval method for both the RAR MTF (subject to assumptions on the MTF's analytical form) and the wave spectrum. In each case, a cost function was numerically minimized. The wave spectrum benefits from the available multiple channels since the underlying wave spectrum must be the same in each case.

The RAR MTF was estimated on a case-by-case basis and the results were compared with theoretical treatments. For the amplitude, we observed higher values than are predicted by theory, with the deviation being largest for HH polarization. For the phase, we observed lower values than are predicted by theory for both VV and HH data. However, the polarization dependence of the RAR MTF, shown by the difference in the imaginary part of the RAR MTF between VV and HH polarization, is in good agreement with the theoretical predictions. This indicates that the polarization term of the total RAR MTF is well-described with the theoretical tilt contribution.

The estimated wave spectra, when forward mapped using the estimated RAR MTF, showed good agreement with the observed cross spectra. Derived wave heights were underestimated for the SIR L-band data when compared with *in situ* measurements. Nevertheless, the inversions were autonomous (*i.e.* without any externally supplied information) and consistent with both the wave model and the DWR spectra.

The additional information channels supplied by multi-frequency/multi-polarization may be used to advantage in deriving improved estimates of the ocean wave spectrum in comparison to single-channel radars. Furthermore, use of the inter-look cross spectrum provides significant advantage for the elimination of speckle noise and the resolution of the ocean wave propagation direction.

7 Acknowledgements

We thank the crew and operators of the CCRS CV-580 SAR for their support in the STARS'94 field program; Lawrence Gray (CCRS) and Cathryn Bjerkelund (CCRS) for assisting with the STARS'94 field work; the BIO Ships Division and the Canadian Coast Guard for their support in deploying the buoys; Roop Lalbeharry (AES) for running CSOWM in hindcast mode and supplying the CSOWM spectra; Ben Holt (JPL) for ensuring correct SIR-C/X-SAR datatake scheduling; and Hartmut Runge (DLR) for ensuring quick access to the X-SAR data.

References

[1] W. Alpers and K. Hasselmann. The two-frequency microwave technique for measuring ocean-wave spectra from an airplane or satellite. *Boundary-Layer Met.*, 13:215–230, 1978.

[2] W. Alpers and C. L. Rufenach. The effect of orbital motions on synthetic aperture radar imagery of ocean waves. *IEEE Trans. Antennas Propagat.*, AP–27:685–690, 1979.

[3] L.A. Breivik, B. Haugse, H. Johnsen, H. E. Krogstad, and M. Reistad. Evaluation of sar wave products. Technical Report 2, DNMI, Norwegian Meteorological Institute, January 1995.

[4] C. Brüning, S. Hasselmann, K. Hasselmann, S. Lehner, and T. Gerling. A first evaluation of ERS-1 synthetic aperture radar wave mode data. *The Global Atm. and Ocean Syst.*, 2(1):61–98, 1994.

[5] C. Brüning, R. Schmidt, and W. Alpers. Estimation of the ocean wave radar modulation function from synthetic aperture radar imaging. *J. Geophys. Res.*, 99:9803–9816, 1994.

[6] B. Engen, H. Johnsen, H. E. Krogstad, and S. F. Barstow. Directional wave spectra by inversion of ERS-1 synthetic aperture radar ocean imagery. *IEEE Trans. Geoscience Rem. Sens.*, 32(2):340–352, 1994.

[7] G. Engen and H. Johnsen. SAR-ocean wave inversion using image cross spectra. *IEEE Trans. Geoscience Rem. Sens.*, 33(4):1047–1056, 1995.

[8] A. D. Goldfinger. Estimation of spectra from speckled images. *IEEE Trans. Aerospace Elec. Sys.*, AES–18:675–681, 1982.

[9] J. F. R. Gower. Layover in satellite SAR imagery of ocean waves. *J. Geophys. Res.*, 88:7719–7720, 1983.

[10] T. Hara and W. J. Plant. Hydrodynamic modulation of short wind-wave spectra due to long waves measured by microwave radar. *J. Geophys. Res.*, 99(C5):9767–9784, 1994.

[11] K. Hasselmann and S. Hasselmann. On the nonlinear mapping of an ocean wave spectrum into a SAR image spectrum and its inversion. *J. Geophys. Res.*, 96(C6):10,713–10,729, 1991.

[12] S. Hasselmann, C. Brüning, K. Hasselmann, and P. Heimbach. An improved algorithm for the retrieval of ocean wave spectra from synthetic aperture radar image spectra. *J. Geophys. Res.*, 101(C7):16,615–16,629, 1996.

[13] S. Jacobsen and K. A. Høgda. Estimation of the real aperture radar modulation transfer function directly from synthetic aperture radar ocean wave image spectra without knowledge of the ocean wave height spectrum. *J. Geophys. Res.*, 99(C7):14,291–14,302, 1994.

[14] R. L. Jordan, B. L. Honeycutt, and M. Werner. The SIR-C/X-SAR synthetic aperture radar system. *IEEE Trans. Geoscience Rem. Sens.*, 33(4):829–839, 1995.

[15] D. P. Kasilingam and O. H. Shemdin. The validity of the composite surface model and its application to the modulation of radar backscatter. *Int. J. Rem. Sens.*, 13:2079–2104, 1992.

[16] M. L. Khandekar, R. Lalbeharry, and V. Cardone. The performance of the Canadian Spectral Ocean Wave Model (CSOWM) during the Grand Banks ERS-1 SAR wave spectra validation experiment. *Atmosphere-Ocean*, 32(1):31–60, 1994.

[17] H. E. Krogstad. A simple derivation of Hasselmann's nonlinear ocean-SAR transform. *J. Geophys. Res.*, 97(C2):2421–2425, 1992.

[18] H. E. Krogstad, O. Samset, and P. W. Vachon. Generalizations of the nonlinear ocean-SAR transform and a simplified SAR inversion algorithm. *Atmosphere-Ocean*, 32(1):61–82, 1994.

[19] C. E. Livingstone, A. L. Gray, R. K. Hawkins, P. W. Vachon, T. I. Lukowski, and M. LaLonde. The CCRS airborne SAR systems: Radar for remote sensing research. *Can. J. Rem. Sens.*, 21(4):468–491, 1995.

[20] F. M. Monaldo and D. R. Lyzenga. On the estimation of wave-slope and wave height variance spectra from sar imagery. *IEEE Trans. Geoscience Rem. Sens.*, GE–24(4):543–551, 1986.

[21] W. J. Plant. The modulation transfer function: Concept and applications. In G. J. Komen and W. A. Oost, editors, *Radar Scattering from Modulated Wind Waves*, pages 173–181, 1989.

[22] W. J. Plant, W. C. Keller, and A. Cross. Parametric dependence of the ocean wave-radar modulation transfer function. *J. Geophys. Res.*, 83:9747–9756, 1983.

[23] R. Romeiser, A. Schmidt, and W. Alpers. A three-scale composite surface model for the ocean wave-radar modulation transfer function. *J. Geophys. Res.*, 99(C5):9785–9801, 1994.

[24] P. W. Vachon and F. W. Dobson. Validation of wind vector retrieval from ERS-1 SAR images over the ocean. *The Global Atm. and Ocean Syst.*, 5:177–187, 1996.

[25] P. W. Vachon, H. E. Krogstad, and J. S. Paterson. Airborne and spaceborne synthetic aperture radar observations of ocean waves. *Atmosphere-Ocean*, 32(1):83–112, 1994.

[26] P. W. Vachon and R. K. Raney. Resolution of the ocean wave propagation direction in SAR imagery. *IEEE Trans. Geoscience Rem. Sens.*, 29(1):105–112, 1991.

Table 1: Summary of SIR-C/X-SAR datatakes over the Gulf of St. Lawrence.

data take	date 1994	time [UTC]	look	track	mode	R/V_p [s]	$\theta_{\rm X}$,$\theta_{\rm C,L}$ [°]	$\tau_{\rm X}$,$\tau_{\rm C}$,$\tau_{\rm L}$ [ms]
17.23	Oct. 1	11:09	left	50°	11x	33	22,23	20,36,153
33.23	Oct. 2	10:51	left	50°	16x	33	23,24	20,36,154
49.33	Oct. 3	10:32	left	51°	16x	33	23,24	20,36,153
65.23	Oct. 4	10:13	left	51°	16x	32	19,20	20,36,153
81.22	Oct. 5	09:53	right	53°	13x	32	22,21	19,35,148
113.4	Oct. 7	09:13	right	54°	13x	36	36,37	27,49,209
mode 11x = L-HH, L-HV, C-HH, C-HV, X-VV								
mode 13x = L-HH, L-VV, C-HH, C-VV, X-VV								
mode 16x = L-VH, L-HH, L-VV, L-HV, C-VH, C-HH, C-VV, C-HV, X-VV								

Table 2: Summary of relevant STARS'94 SAR data over the Grand Banks.

date 1994	time [UTC]	look	track	mode	R/V_p [s]	θ [°]	τ [ms]
Dec. 3	14:32	right	195°	ERS-1	115	22	316
	15:05	left	137°	dual pol.	25	55	547
Dec. 4	01:50	right	345°	ERS-1	115	22	316
	02:13	left	137°	dual pol.	36	67	782
Dec. 5	23:30	left	130°	dual pol.	38	53	831

Table 3: RAR MTF Measurements (theoretical values in parenthesis).

data set	amplitude		phase		real part	imag. part		difference	Bragg	wind growth
	VV	HH	VV	HH	VV & HH	VV	HH	$b_{\rm VV}-b_{\rm HH}$	wavenumber	rate
CV-580 C-band, Dec. 3	16.6	17.9	10.6°	24.6°	1.10	0.21	0.50	-0.29	135 rad/m	$0.35\,{\rm s}^{-1}$
	(2.3)	(7.3)	(0.8°)	(71.6°)	(0.16)	(0.00)	(0.47)	(-0.47)		
CV-580 C-band, Dec. 4	19.7	31.4	36.4°	59.7°	0.88	0.65	1.50	-0.85	93 rad/m	$0.13\,{\rm s}^{-1}$
	(3.6)	(10.7)	(−1.9°)	(70.5°)	(0.20)	(-0.01)	(0.55)	(-0.56)		
CV-580 C-band, Dec. 5	12.8	18.4	23.6°	50.3°	0.79	0.35	0.95	-0.60	142 rad/m	$0.03\,{\rm s}^{-1}$
	(4.3)	(9.4)	(26.0°)	(64.8°)	(0.27)	(0.13)	(0.57)	(-0.44)		
SIR L-band, Oct. 2	15.9	17.3	44.3°	48.7°	1.05	1.03	1.20	-0.17	48.8 rad/m	$0.45\,{\rm s}^{-1}$
	(7.1)	(10.0)	(72.7°)	(77.9°)	(0.19)	(0.62)	(0.90)	(-0.28)		
SIR L-band, Oct. 3	14.4	15.8	37.2°	43.4°	1.26	0.96	1.19	-0.23	48.0 rad/m	$0.70\,{\rm s}^{-1}$
	(7.0)	(10.0)	(78.3°)	(81.8°)	(0.16)	(0.76)	(1.09)	(-0.33)		
SIR L-band, Oct. 7	9.7	11.1	38.5°	46.8°	0.89	0.70	0.94	-0.24	42.5 rad/m	$0.35\,{\rm s}^{-1}$
	(7.2)	(11.3)	(67.0°)	(75.6°)	(0.33)	(0.77)	(1.27)	(-0.50)		

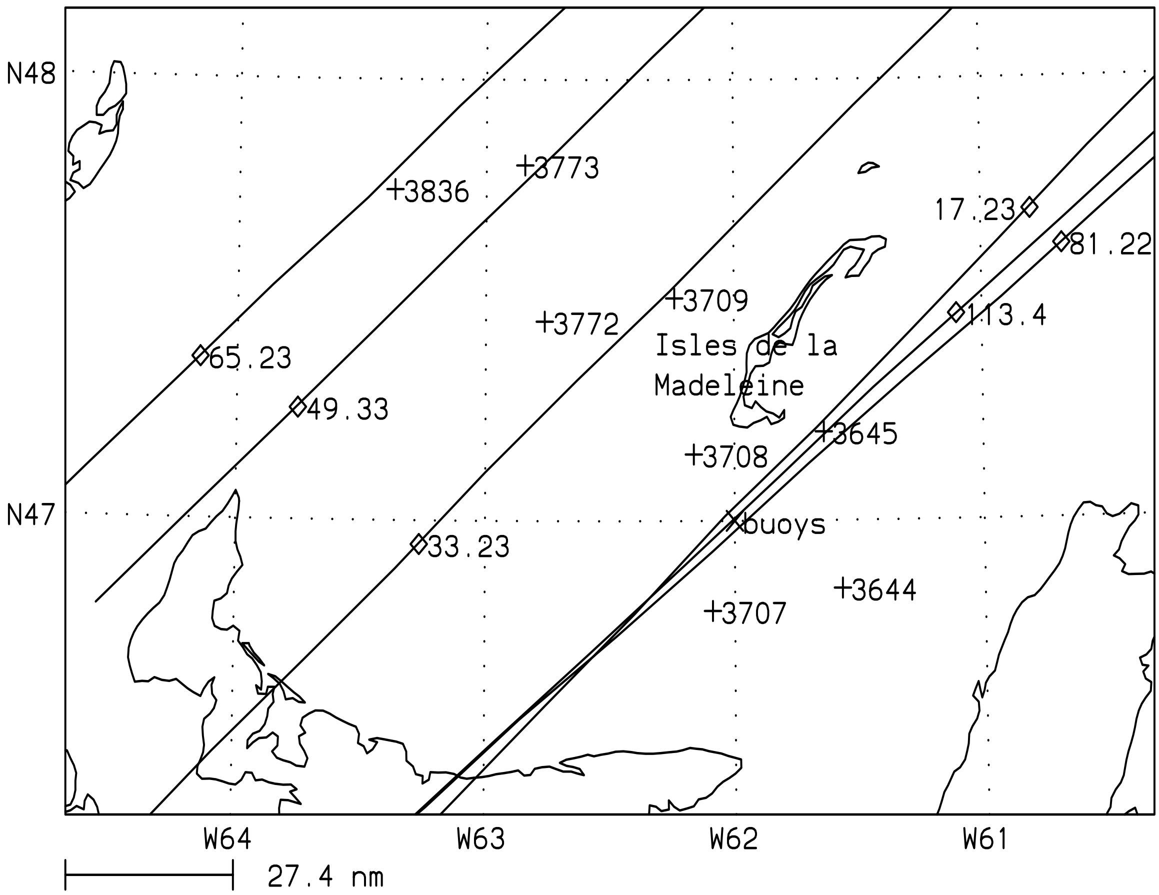

Figure 1: Map of the Gulf of St. Lawrence experiment site. Buoy location (×), key CSOWM grid points (+) (labelled by number), and the SIR-C image centrelines (solid lines) for the SIR-C/X-SAR datatakes are indicated.

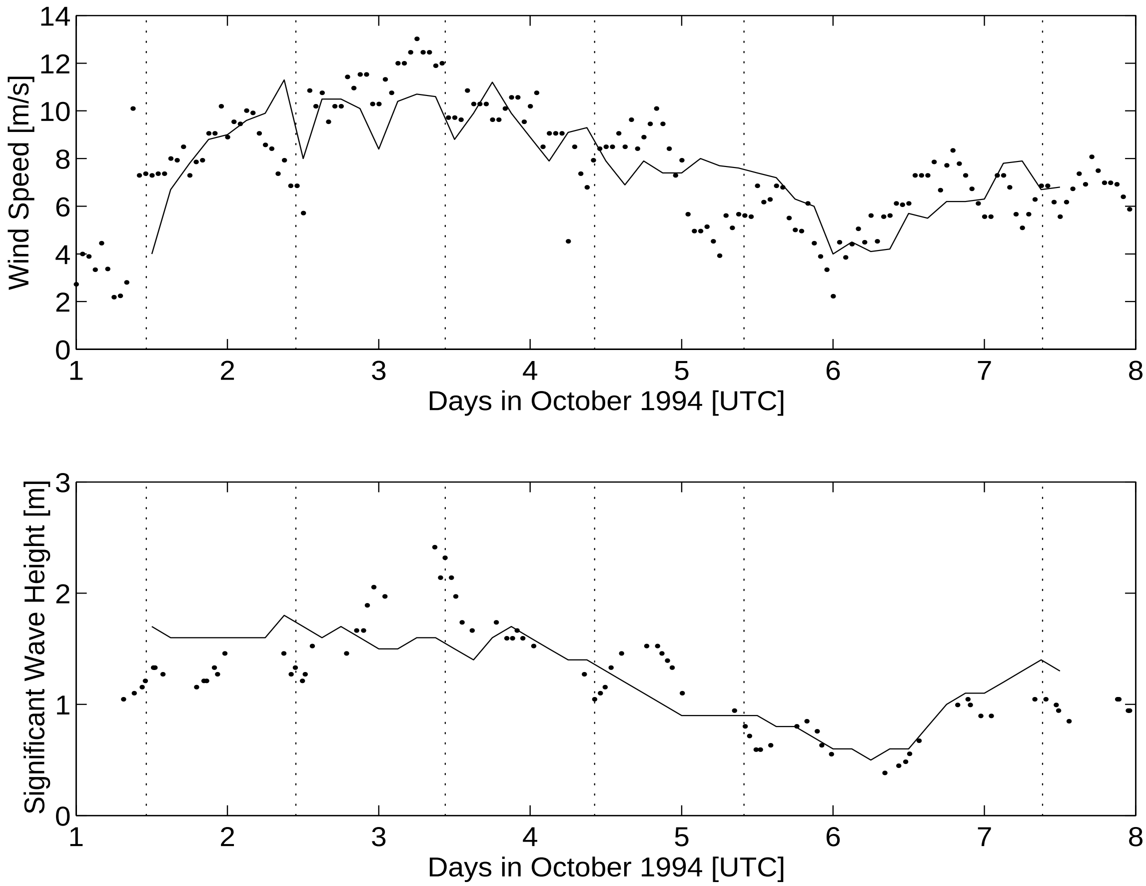

Figure 2: Time series of wind speed U_{10}^{N} (upper) and significant wave height H_s (lower) for the Gulf of St. Lawrence site. CMC surface wind field and CSOWM wave height (solid lines, for grid point 3708) and MM and DWR buoys (dots) are compared. The vertical dotted lines indicate the times of the SIR-C/X-SAR datatakes.

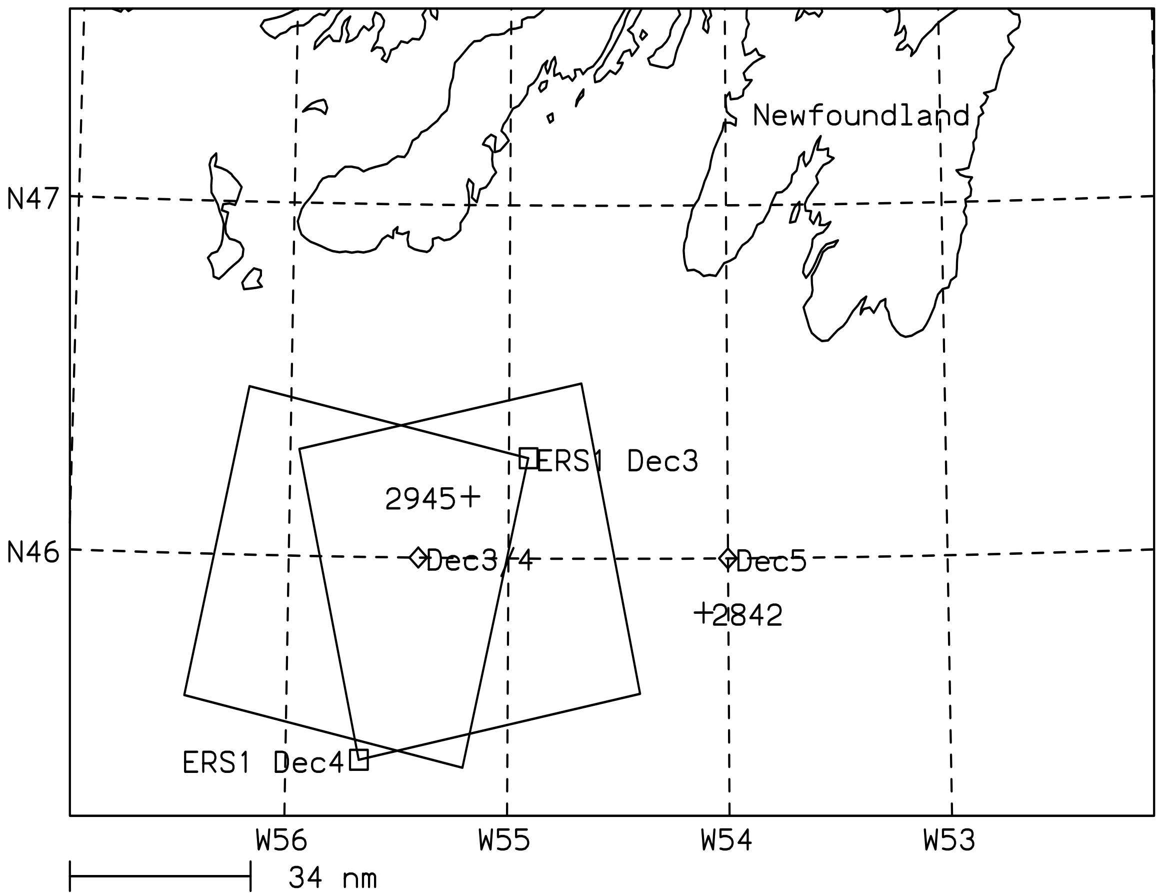

Figure 3: Map of the Grand Banks of Newfoundland experiment site. CSS *Parizeau* locations on Dec. 3/4, and 5, and key CSOWM grid points (+) (labelled by number) are indicated. The DWR was near the point marked Dec. 3/4 while the MM was near the point marked Dec. 5. The frames indicate the extent of ERS-1 SAR coverage on Dec. 3 and 4.

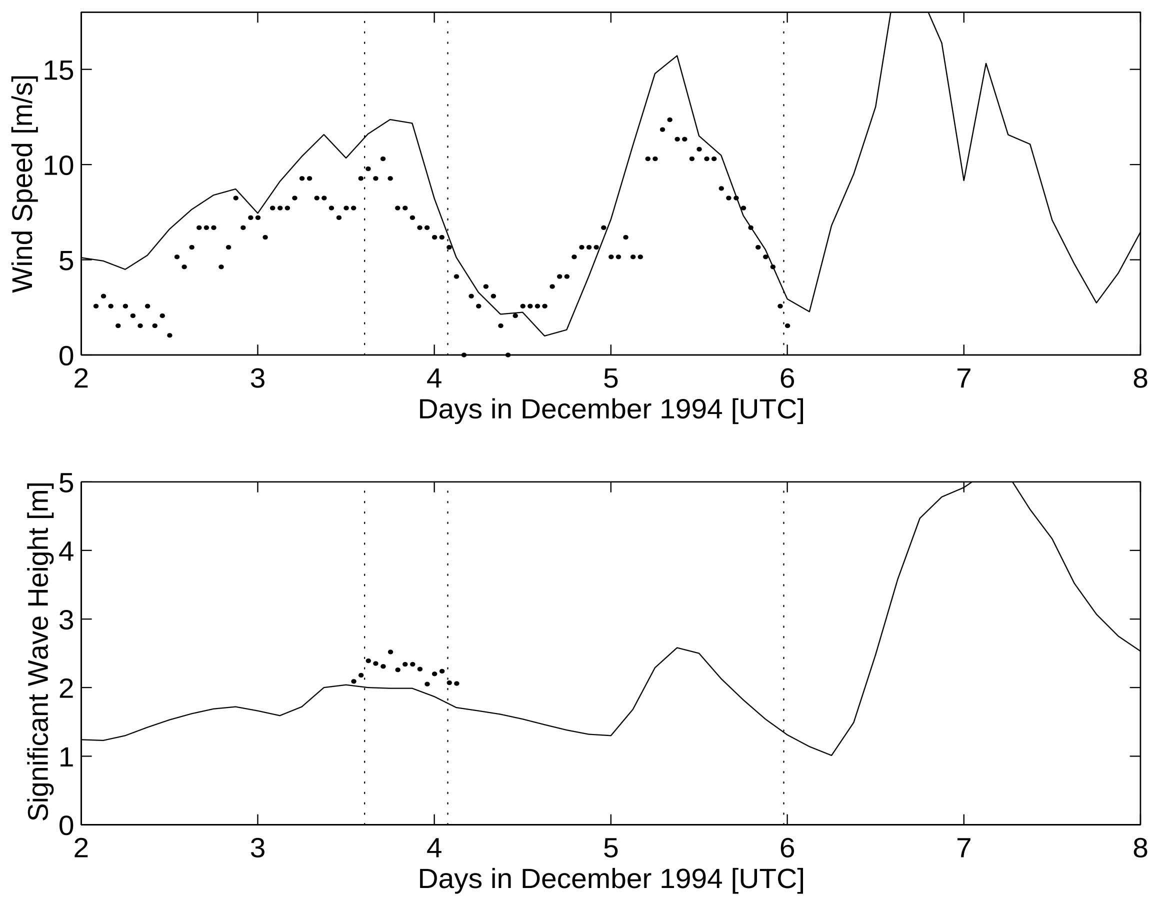

Figure 4: Time series of wind speed U_{10}^{N} (upper) and significant wave height H_s (lower) for the Grand Banks site. Surface wind field (for grid point 2842) and CSOWM wave height (for grid point 2945) (solid lines) and MM and DWR buoys (dots) are compared. The vertical dotted lines indicate the times of the CV-580 SAR flights.

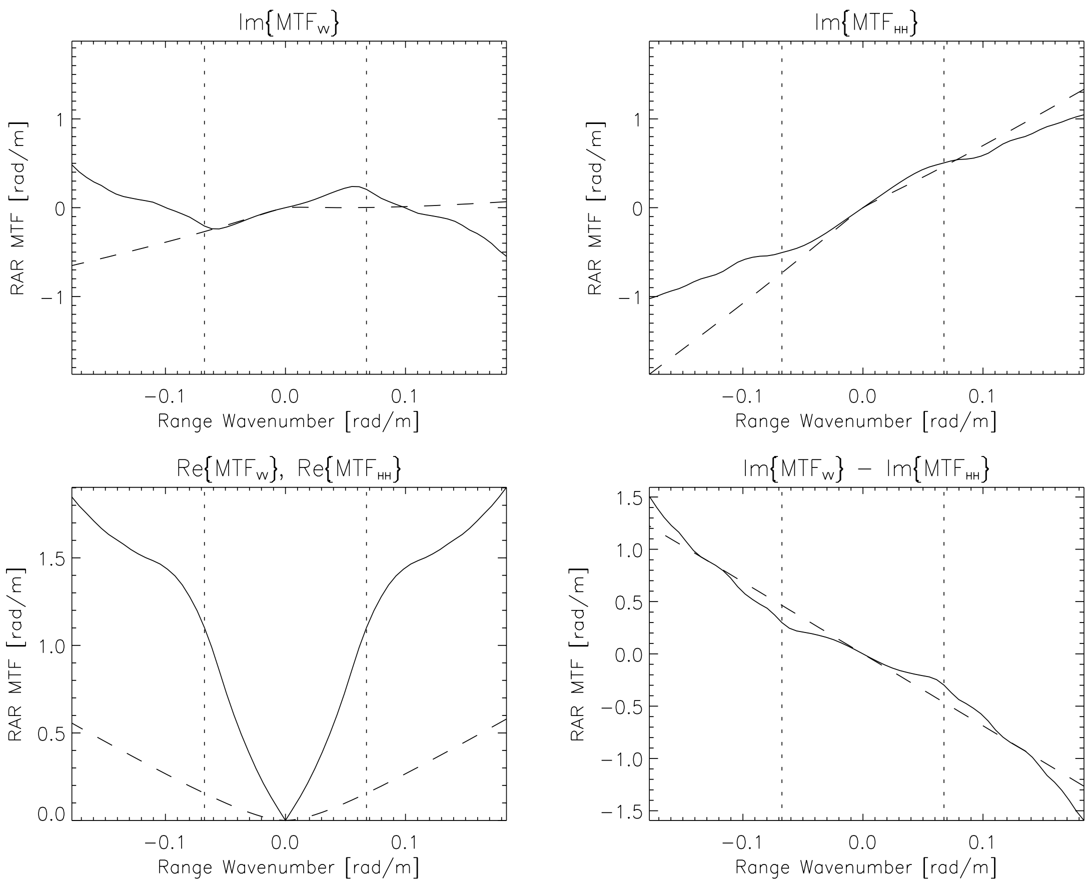

Figure 5: Theoretical and estimated RAR MTFs for CV-580 C-band, Dec. 3. Upper plots: imaginary part of the VV and HH polarization MTFs. Lower left: the real parts of the MTFs. Lower right: the difference of the imaginary parts between the VV and HH polarization MTFs (solid line - estimated; dashed line - theoretical). The vertical dotted line shows the location of the spectral maximum along the range axis.

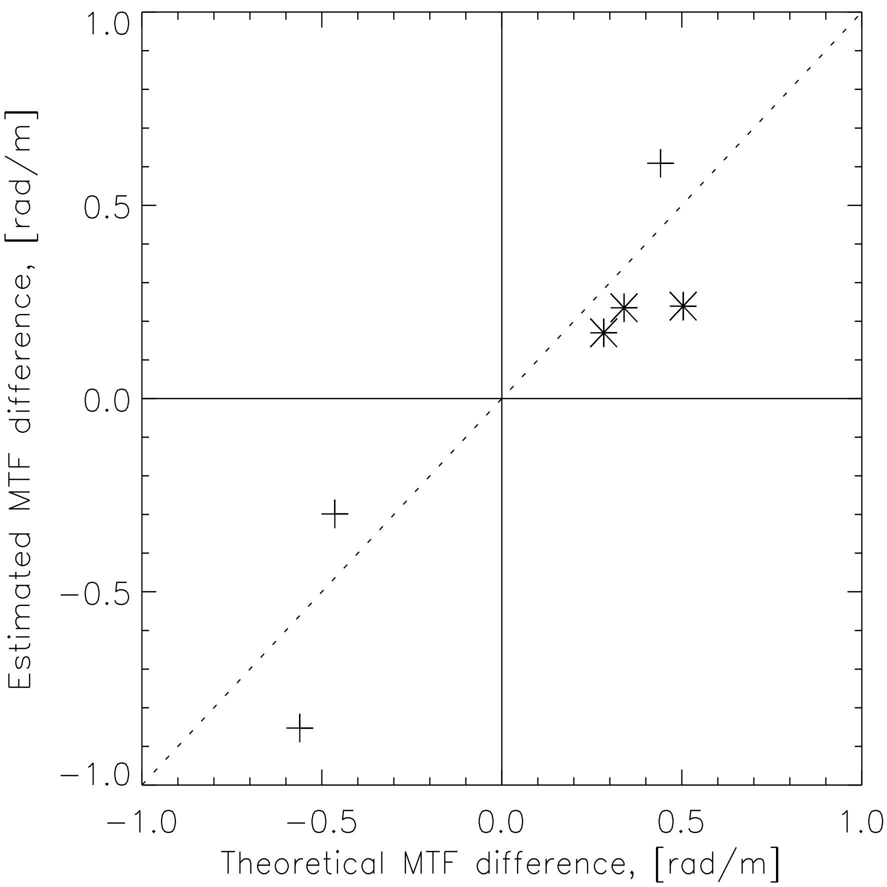

Figure 6: Theoretical and estimated difference of the imaginary part of the VV and HH polarization RAR MTF. The measured points are for the spectral maxima along the range wavenumber axis. + corresponds to CV-580 C-band data, and * corresponds to SIR L-band data.

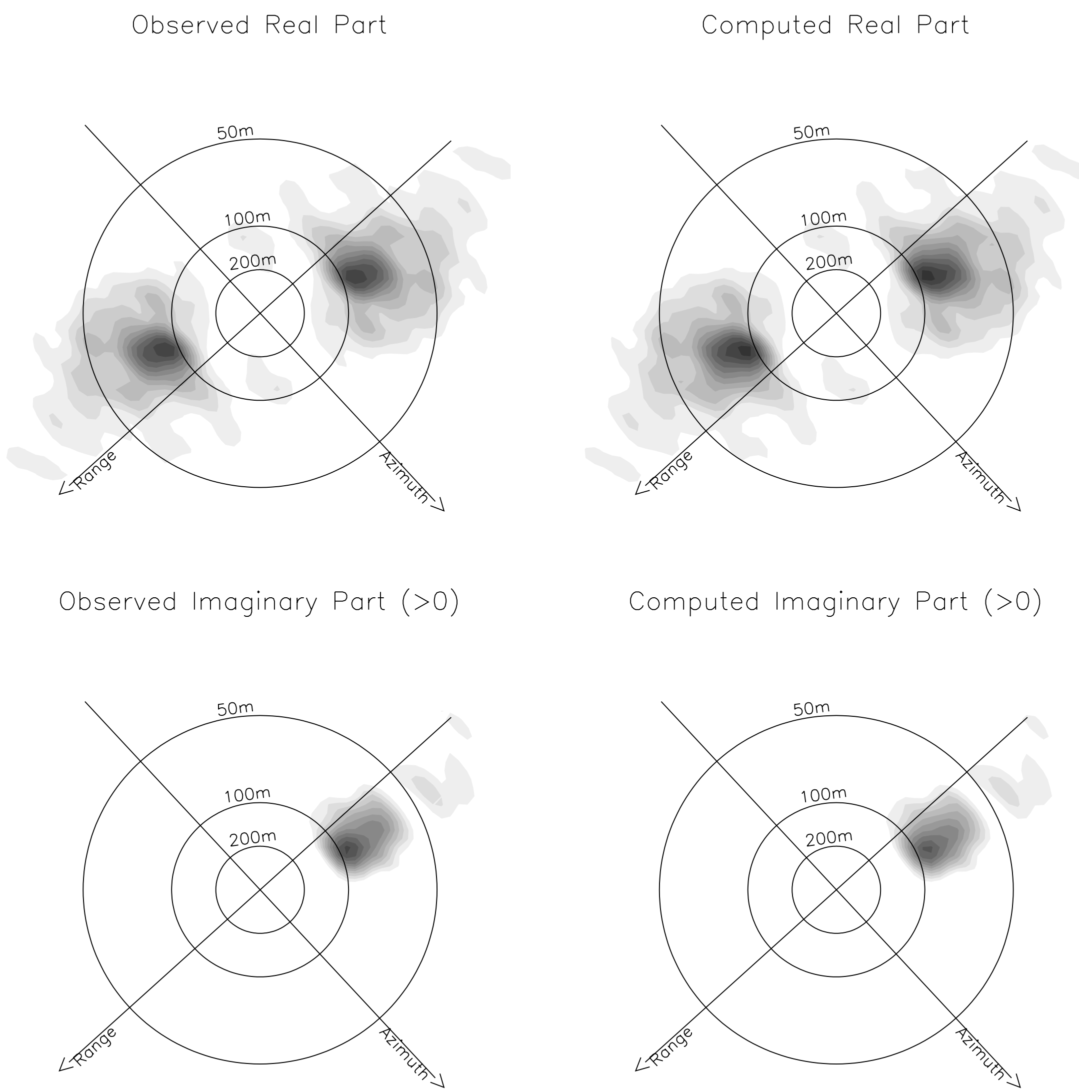

Figure 7: Observed average SAR cross spectrum and computed SAR cross spectrum for CV-580 C-band, Dec. 3.

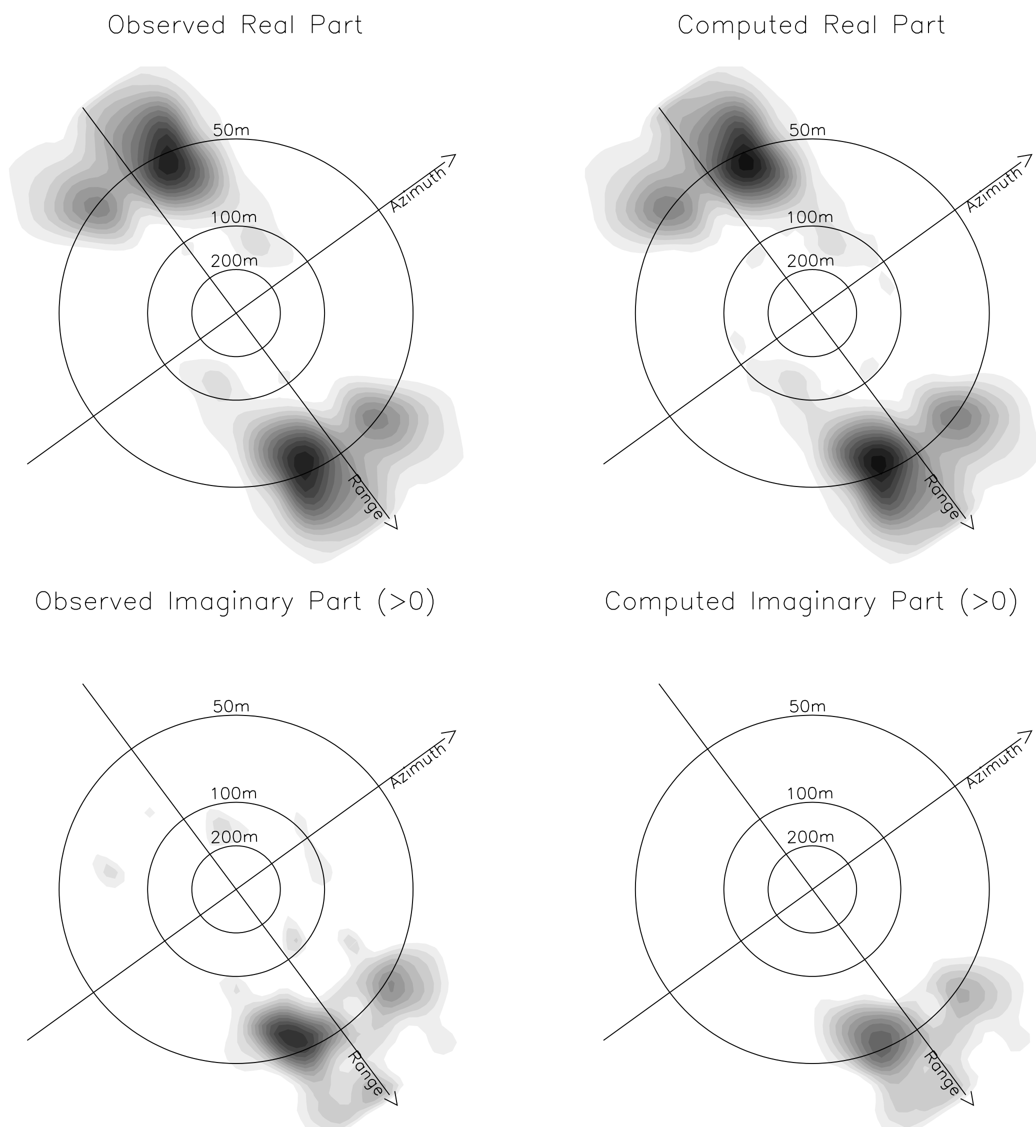

Figure 8: Observed average SAR cross spectrum and computed SAR cross spectrum for SIR L-band, Oct. 7.

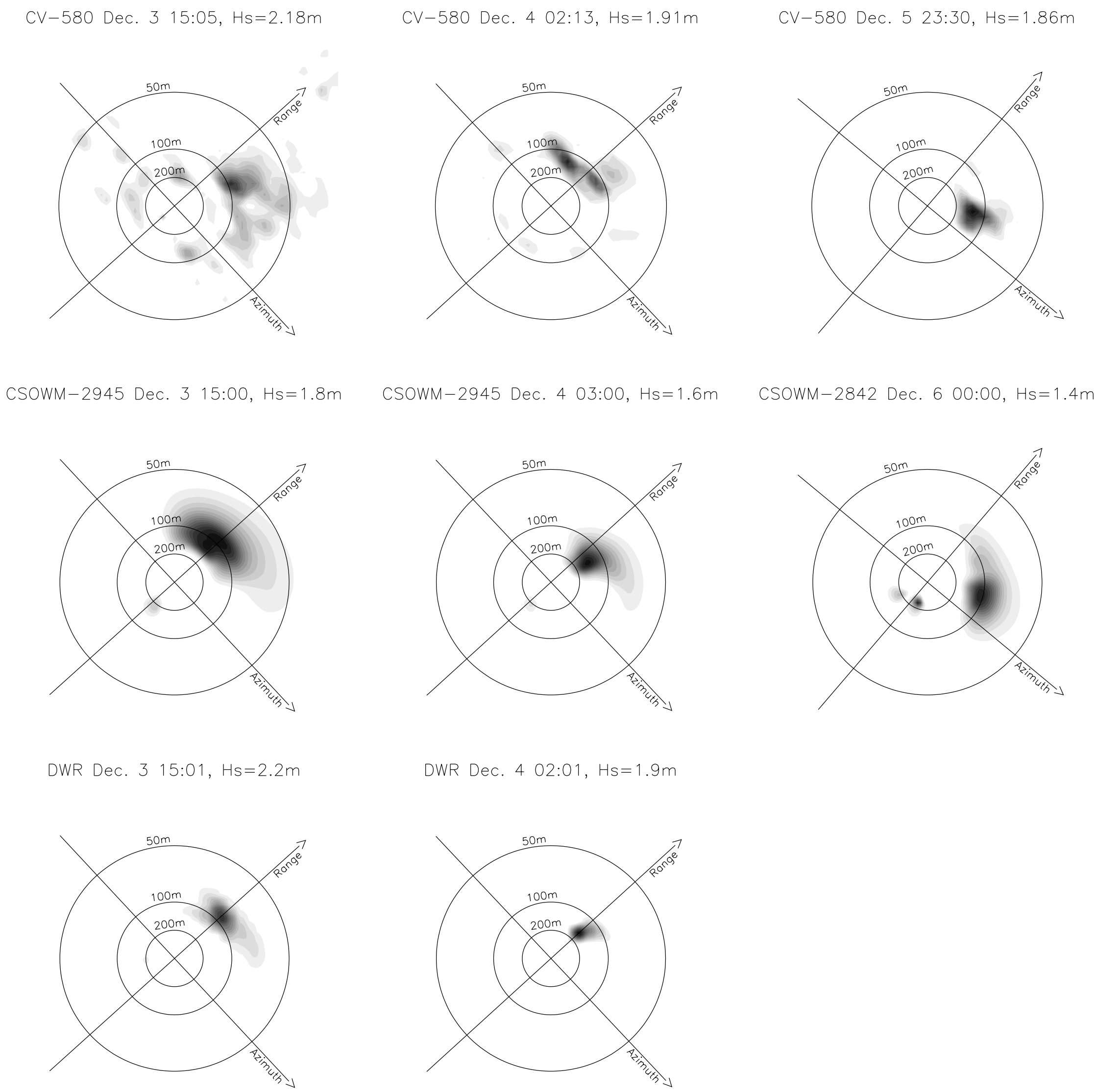

Figure 9: Estimated ocean wave spectra from CV-580 C-band (upper), CSOWM wave model (mid), and DWR buoy (lower). Hs refers to the significant wave height.

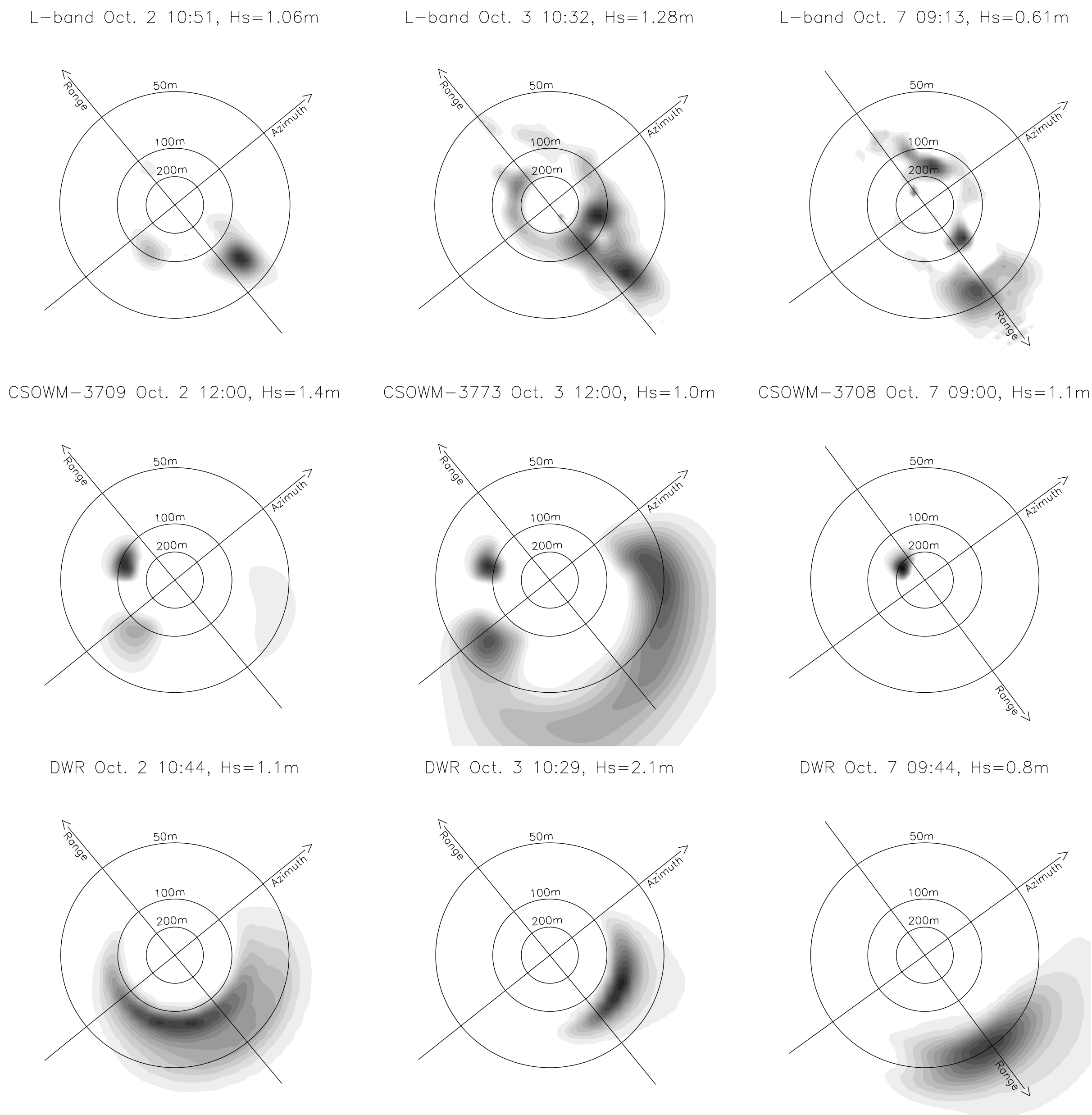

Figure 10: Estimated ocean wave spectra from SIR L-band (upper), CSOWM wave model (mid), and DWR buoy (lower). Hs refers to the significant waveheight.

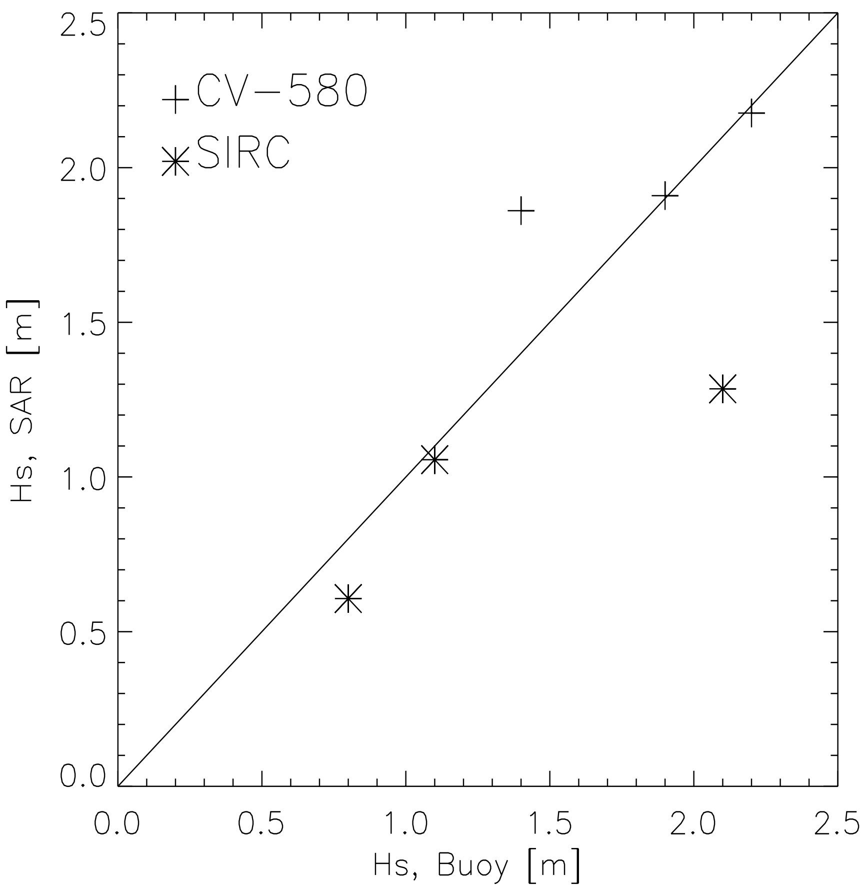

Figure 11: Significant waveheight for buoy vs. SAR. + refers to CV-580 C-band data, and * refers to SIR L-band data.

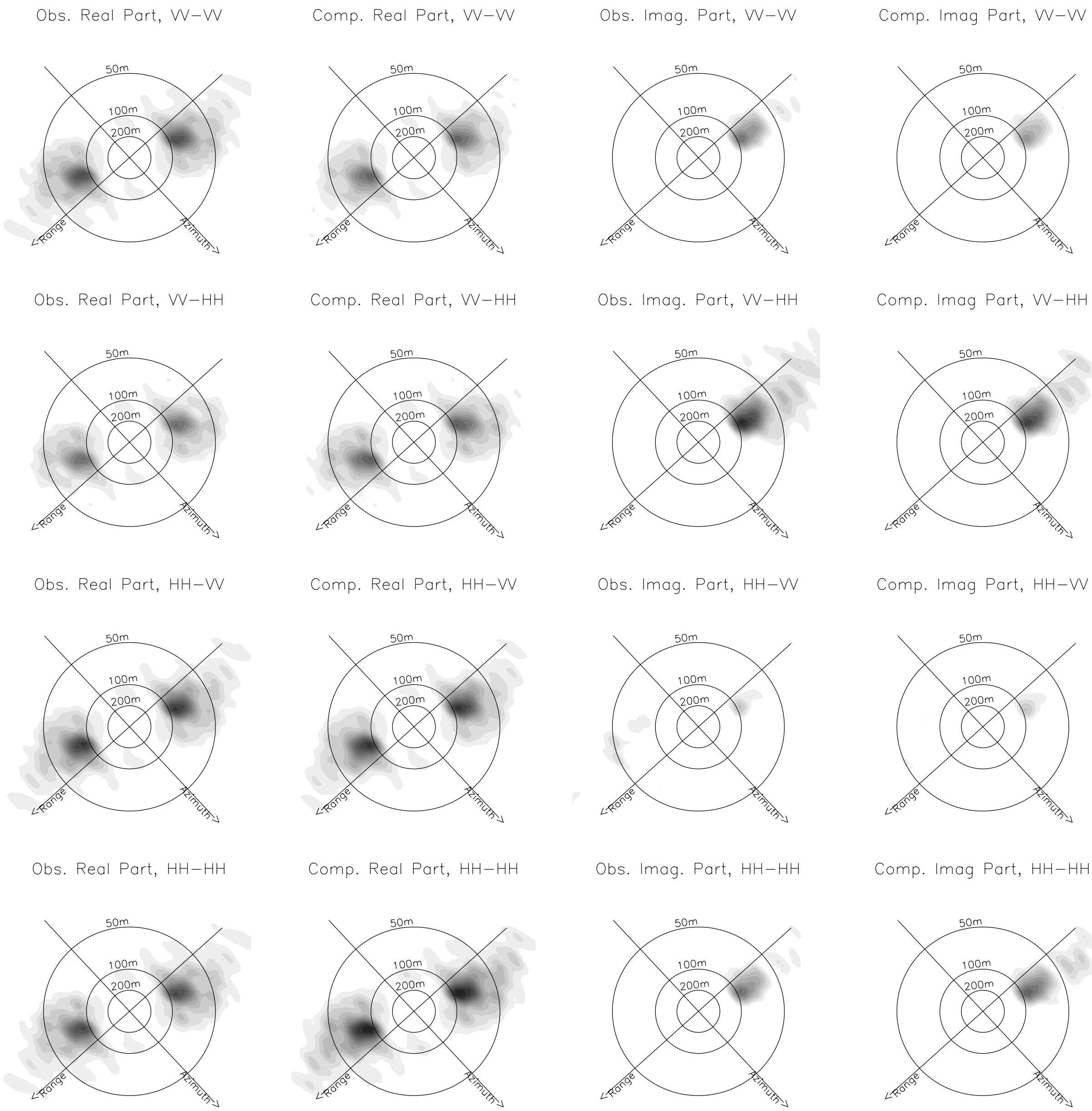

Figure 12: Observed and computed SAR spectra for CV-580 C-band, Dec. 3.

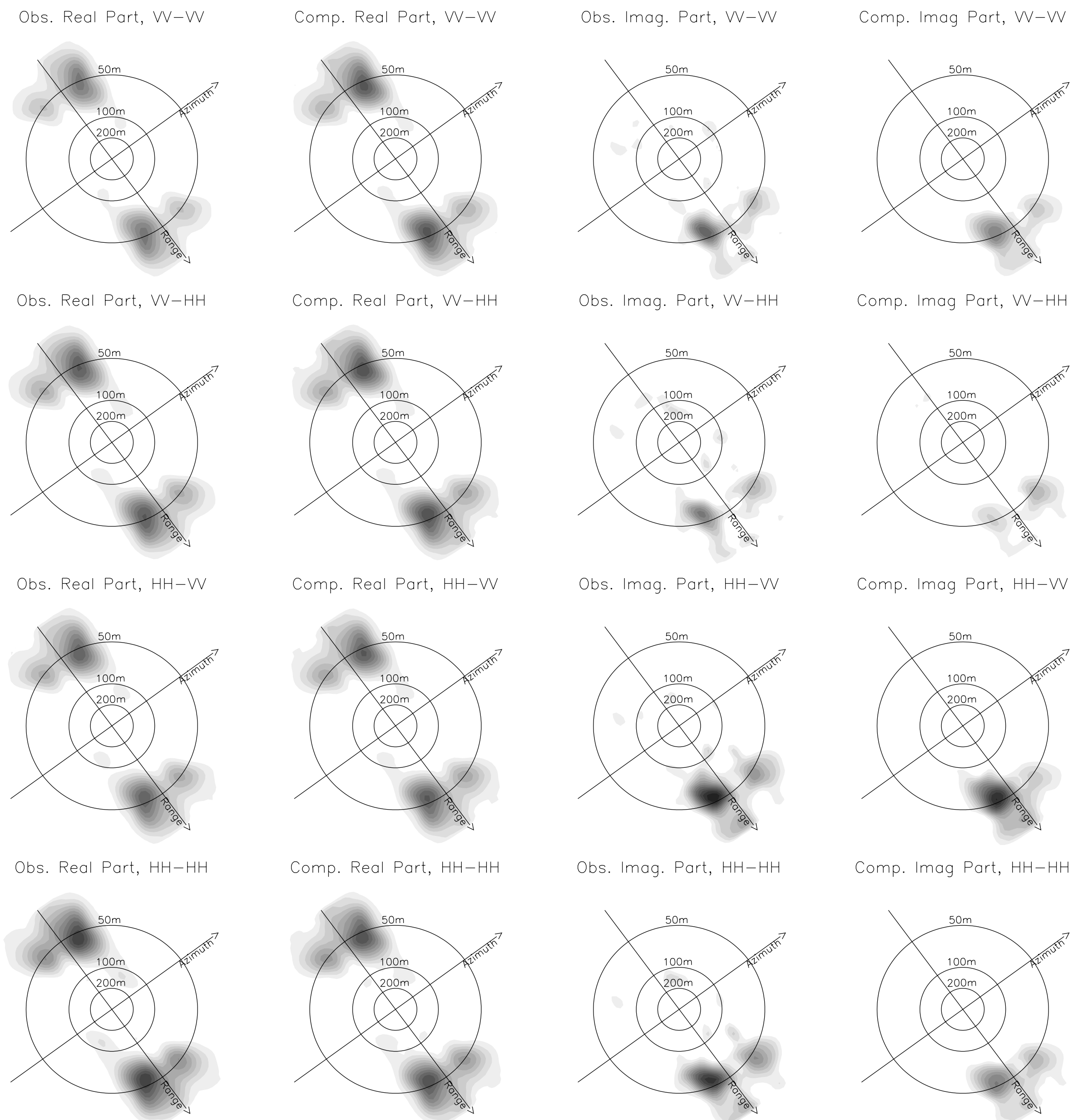

Figure 13: Observed and computed SAR spectra for SIR L-band, Oct. 7.